Space Weather

Key Points:
- Usage of a standard distribution function, like a single Maxwellian, to reconstruct plasma sheet electron fluxes is only good below 10 keV
- A kappa, and in some cases two population distributions, gives a better fit, with the kappa parameter strongly depending on location
- The error with observed fluxes can be large, implying that a more advanced model is needed, based on flux instead of distribution moments

Supporting Information:
- Supporting Information S1

Correspondence to:
S. Dubyagin,
stepan.dubyagin@fmi.fi

On the Accuracy of Reconstructing Plasma Sheet Electron Fluxes From Temperature and Density Models

S. Dubyagin[1] , N. Ganushkina[2] , and M. Liemohn[2]

[1]Finnish Meteorological Institute, Helsinki, Finland, [2]Climate and Space Science and Engineering Department, University of Michigan, Ann Arbor, MI, USA

Abstract The particle simulations of the inner magnetosphere require time-dependent boundary conditions for the particle flux set in the transition region between dipolar and tail-like configurations. Usually, the flux is reconstructed from particle density and temperature predicted by empirical models or magnetohydrodynamic simulations. However, this method requires assumptions about the energy spectra to be made. This uncertainty adds to the inaccuracy of the empirical models or magnetohydrodynamic predictions. We use electron flux measurements in the nightside at $r = 6–11R_E$ in the 1–300 keV energy range to estimate the potential accuracy of the electron flux reconstruction from the macroscopic plasma parameter models. We use kappa and Maxwellian distribution functions as well as two population approximations to describe the electron spectra. It is found that this method works reasonably well in the thermal energy range (1–10 keV). However, the average difference between measured and predicted fluxes becomes as large as 1 order of magnitude at energies ≥40 keV. The optimal value of the kappa parameter is found to be between 3 and 4, but it depends strongly on magnetic local time and radial distance. We conclude that the development of the flux-based models (model of differential flux at several reference energies) instead of density and temperature models can be considered as a promising direction.

1. Introduction

The high fluxes of superthermal electrons in the inner magnetosphere may lead to malfunction or even permanent damage of expensive spacecraft on MEO and GEO orbits. The fluxes dramatically increase during the periods of magnetospheric disturbance such as geomagnetic storms and substorms. The prediction of their evolution during such events is a challenging task, and various particle simulations of the inner magnetosphere are aimed to solve it (Buzulukova et al., 2010; Chen et al., 2006; Fok et al., 2001, 2014; Ganushkina et al., 2013, 2014; Harel et al., 1981; Jordanova et al., 2014; Jordanova & Miyoshi, 2005; Toffoletto et al., 2003). These simulations solve physical equations of the particle statistical mechanics in the inner magnetosphere under different assumptions and at a different level of sophistication. What is common for all these simulations is that their computational domain is confined within the inner magnetosphere and they require the particle fluxes set at the outer boundary of the simulation domain, which is usually placed between geosynchronous orbit and $r \approx 10R_E$. It should be noted that the accuracy of the flux boundary condition to a large extent defines the performance of simulation itself, as was recently demonstrated by Yu et al. (2019).

At least for some periods, the fluxes can be observed in real time by the geostationary or magnetospheric spacecraft and passed as a boundary condition to the simulation. Although this method has been widely used in magnetospheric studies (e.g. Fok et al., 2001; Ganushkina et al., 2006; Jordanova et al., 2003, 2003), it has limited application for forecasting purposes. Even if a few geostationary spacecraft cover a wide magnetic local time (MLT) sector, nonzero magnetic latitude of a spacecraft results in high L-shells values, and sometimes a spacecraft can be even in the magnetotail lobes (Thomsen et al., 1994). In addition, the short distance between the observing spacecraft and the radiation belt and ring current region leaves too short of a time (a few minutes) for satellite operators to respond to sudden changes in the predicted environmental conditions (not to mention that, in this case, it is impossible to forecast conditions at geosynchronous orbit). In this respect, the empirical models or global magnetohydrodynamic (MHD) simulations driven by the solar wind parameters observed at the L1 Lagrangian point are much more advantageous; they can output

Construction of the boundary conditions for particle simulations of the inner magnetosphere
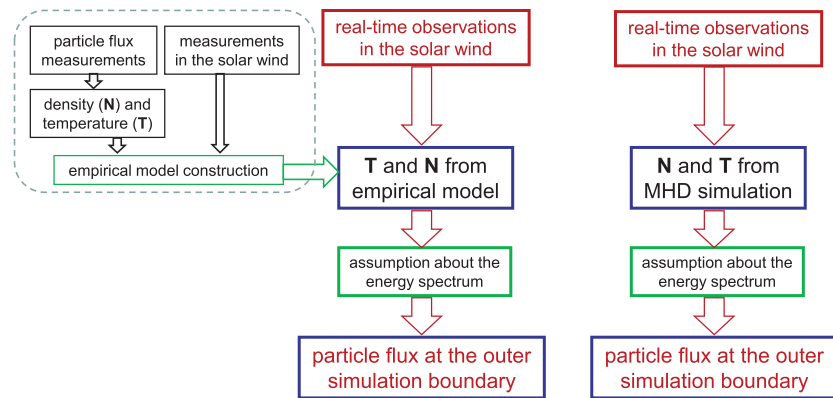
Figure 1. The block diagram shows two schemes of the boundary condition construction.

estimated plasma parameters at any spatial location at least tens of minutes before the actual disturbance impacts the magnetosphere.

The block diagram in Figure 1 shows two widely used schemes of the flux boundary condition construction for the inner magnetosphere simulation. The solar wind observations at the L1 point (red block) provide input for an empirical model of the macroscopic plasma parameters (left part) or MHD simulation (right part). The empirical model or MHD simulation outputs the density and temperature values which can be used to calculate the particle flux under assumptions of certain forms of the particle energy spectrum. The empirical models are built from the big volume of historical data and represent averaged dependencies of the macroscopic plasma parameters on solar wind drivers. The blocks surrounded by the dashed frame in the left part of Figure 1 demonstrate schematically the process of the empirical model development. It can be seen that the flux data are used first to compute the temperature and density, and the information about energy spectrum is being lost at this step. On the other hand, the plasma sheet density and temperature are easier to model (in comparison to particle flux) because they obey relatively simple MHD equations, and hence, their dependencies on solar wind drivers are also simpler. If MHD simulation is used for boundary condition construction, the plasma density and temperature are the only available parameters characterizing properties of the plasma population. Eventually, both boundary condition construction schemes end up with a need to make an assumption about the energy spectrum to calculate the flux from the density and temperature (green block in Figure 1). However, making a right assumption is a hard task because the particle spectrum observations in the magnetosphere have revealed that non-Maxwellian distributions of ions and electrons are common in the plasma sheet (e.g., Åsnes et al., 2008; Christon et al., 1989; Christon et al., 1991; Espinoza et al., 2018; Vasyliunas, 1968), and the populations with different temperatures can be present simultaneously (Walsh et al., 2013; Wang et al., 2007; Wing et al., 2005). Thus, this assumption introduces inaccuracy into the flux values which is summed up with the inaccuracy of the temperature and density model predictions. The purpose of our study is to analyze quantitatively this inaccuracy and to outline the possible strategies for improvements of the boundary condition construction schemes.

In this paper, we analyze a large data set of the electron spectra observations on board three Time History of Events and Macroscale Interactions during Substorms (THEMIS) probes in the transition region of the magnetosphere during geomagnetic storms. We intentionally concentrate on geomagnetic storm periods because they are the main targets of inner magnetosphere modeling. The observed differential flux spectra are used to assess the possible errors of the flux estimated from the temperature and density values for commonly used energy distributions. The electron temperature and density are estimated using Dubyagin et al. (2016) model and also calculated from the observed flux spectra themselves. The paper is organized as follows: in section 2 we describe the data set. In section 3, we compare the directly measured flux and that estimated from the density and temperature values. Then, in section 4 we fit the observed spectra using single- and two-population distributions and analyze the occurrence of these two types of spectra. In addition, we investigate statistically the observed spectra and use this information to discuss the possible strategies to improve

electron flux prediction abilities of the empirical models and MHD simulations in sections 6. Finally, the conclusions are made in section 7.

2. Data

In the present study, the particle detector measurements on board the Time History of Events and Macroscale Interactions during Substorms (THEMIS) mission (Angelopoulos, 2008) are used to calculate the energy spectra and distribution function moments. We use the same data set that was used by Dubyagin et al. (2016) for the empirical model of the electron temperature and density construction. The detailed data and event selection descriptions can be found in the original paper, and we will only briefly summarize them here. We use the data of three THEMIS probes (A, D, and E) on the nightside in the radial distance range of $6-11R_E$. These data were collected during all storms with min SYM-H < -50 nT that took place in the years 2007–2013. The fluxgate magnetometer measurements (Auster et al., 2008) were used to select the observations in the vicinity of the neutral sheet as described in Dubyagin et al. (2016). The density and temperatures as well as the energy spectra were computed from the combined velocity distributions measured by Solid State Telescope (SST) (Angelopoulos et al., 2008) and Electrostatic Analyzer (ESA) (McFadden et al., 2008; McFadden et al., 2008) covering $\sim$ 30 eV to 300 keV energy range at spin resolution (3 s). These data were then averaged over 1.6 min intervals. The temperature tensor and density were computed using THEMIS software (http://themis.ssl.berkeley.edu/software.shtml), and the differential energy flux was averaged over 45–135° pitch angles. The resulting data set comprises 32,008 records of plasma sheet electron spectra, density and electron perpendicular temperature complemented by values of the magnetic field and plasma parameters in the solar wind. The fewer number of data records in comparison to the Dubyagin et al. (2016) data set is due to the events with absent measurements for some energy channels inside one 1.6 min interval. The plasma moments, which were used in Dubyagin et al. (2016), could be computed for such events, but the spectra could not be averaged using simple methods for such intervals and were discarded. The SST energy channels above $\sim$100 keV sometimes reveal flat (or even having positive slope) electron spectra which are likely a result of contamination from higher energy particles. In supporting information Text S1, we describe the automatic method to detect and clean such spectra (this problem was detected for 18% of data).

For an isotropic particle distribution with no bulk velocity present, the temperature (T) and number density (N) can be computed as numerical integrals of the measured energy flux over the particle detector energy range:

$$N = 2^{\frac{3}{2}} \pi \sqrt{m} \int \frac{J_E}{E^{\frac{3}{2}}} \mathrm{d}E \ , \tag{1}$$

$$P = 4\pi \frac{\sqrt{2}}{3} \sqrt{m} \int \frac{J_E}{\sqrt{E}} \mathrm{d}E \ , \tag{2}$$

$$T = \frac{P}{N}. \tag{3}$$

where P is the plasma pressure, J_E is the measured differential energy flux averaged over all directions, and m and E are the particle mass and energy, respectively. However, particle distributions in the inner magnetosphere are generally anisotropic; therefore, the generalized forms of equations (1)–(3) should be used, where T and P are tensors and integration in equations (1) and (2) is performed over the whole (3-D) velocity space (in spherical coordinate system) as described in Paschmann and Daly (1998). On the other hand, gyrotropy is a good approximation for the electron distributions in the inner magnetosphere, and the full pressure/temperature tensor can be reduced to the parallel and perpendicular components, which are computed by tensor rotation to the coordinate system based on magnetic field vector direction. This approach is implemented in the THEMIS software for the plasma moments computation (the software also removes contaminations and calibrates the data).

Figure 2 shows the histograms of perpendicular electron temperature and number density computed by the THEMIS software from the flux measurements. It can be seen that the temperature histogram has an additional peak at small $T_{\perp e}$ values. These measurements correspond to the events when additional dense
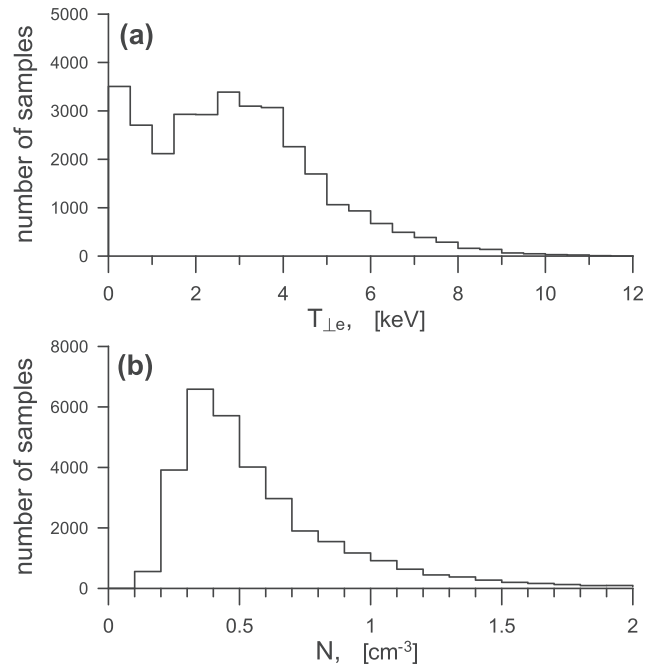
Figure 2. The histograms of temperature (a) and density (b) computed from THEMIS data.

cold population is present. Since the temperature is computed as a ratio of pressure to density (equation (3)), the presence of a dense cold population results in a very low temperature value. At the same time, the temperature of the hot population can be rather high, and the fluxes at the high energies are much higher than expected if only a nominal temperature value is considered and a single distribution function is used for the spectrum approximation.

In addition to the THEMIS plasma moments, we use Dubyagin et al. (2016) empirical model of the electron temperature and density. The model outputs the temperature and density in the equatorial plane as a function of location and time-integrated solar-wind plasma and magnetic field parameters. The precomputed input parameters of the model as well as the script calculating these parameters from OMNI database can be found in the supporting information section of Dubyagin et al. (2016). The model was specifically designed to make prediction during geomagnetic storms for $r = 6\text{–}11 R_E$ on the nightside and, in spite of its simplicity, shows good performance with correlation coefficient between the real parameters and model predictions CC = 0.82 for the density and CC = 0.76 for the temperature predictions.

3. Comparison of Measured Particle Flux With That Calculated From Temperature and Density

In order to compute the electron flux from the density and temperature values, we use two energy distribution forms, namely, Maxwellian and kappa (e.g. Livadiotis, 2015; Xiao et al., 2008) distributions:

$$f(E)^{maxwell} = N \left(\frac{m}{2\pi T} \right)^{\frac{2}{3}} \exp \left(-\frac{E}{T} \right), \tag{4}$$

$$f(E)^{kappa} = N \left(\frac{m}{\pi (2\kappa - 3) T} \right)^{\frac{2}{3}} \frac{\Gamma (\kappa + 1)}{\Gamma \left(\kappa - \frac{1}{2} \right)} \left(1 + \frac{2E}{(2\kappa - 3) T} \right)^{-(\kappa+1)}, \tag{5}$$

where κ is the kappa parameter, Γ is the gamma function (extension of factorial function), and the temperature is in the energy units (i.e., multiplied by Boltzmann constant). Using these distributions, the differential energy flux (J_E) can be computed for a given energy, N, T, and κ as
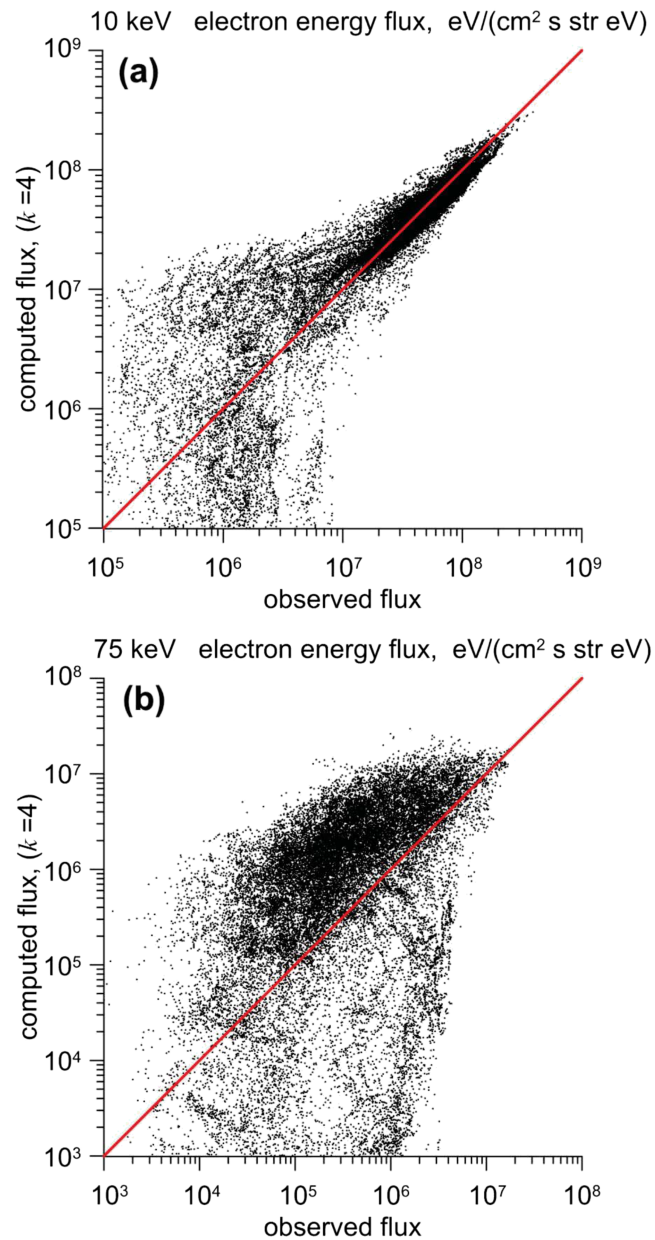
Figure 3. The scatter plot of the measured differential energy flux versus that reconstructed from density and temperature for the kappa distribution ($\kappa = 4$). Panels (a) and (b) correspond to 10 keV and 75 keV energies, respectively.

$$J_E = f(E)\frac{2E^2}{m^2} \tag{6}$$

We start our analysis using this equation to calculate the flux values for N and $T_\perp$, which in turn were computed by THEMIS software from the THEMIS flux measurements. That is, we perform spectra-moments-spectra conversion whereby the information about the actual form of the spectra is lost at the first step and then replaced by the assumed distribution functions at the second step. In Figure 3a, we show the scatter plot of differential energy flux measured at $E = 10$ keV versus that reconstructed from the density and temperature for kappa distribution using equation (6) ($\kappa = 4$ was used because it represents an average value in the near-Earth magnetotail (Espinoza et al., 2018; Runov et al., 2015)). Although such comparison may seem strange, since the reconstructed fluxes eventually are calculated from the fluxes they are compared to, it can give us an idea of what is the best result we can expect from an empirical model if
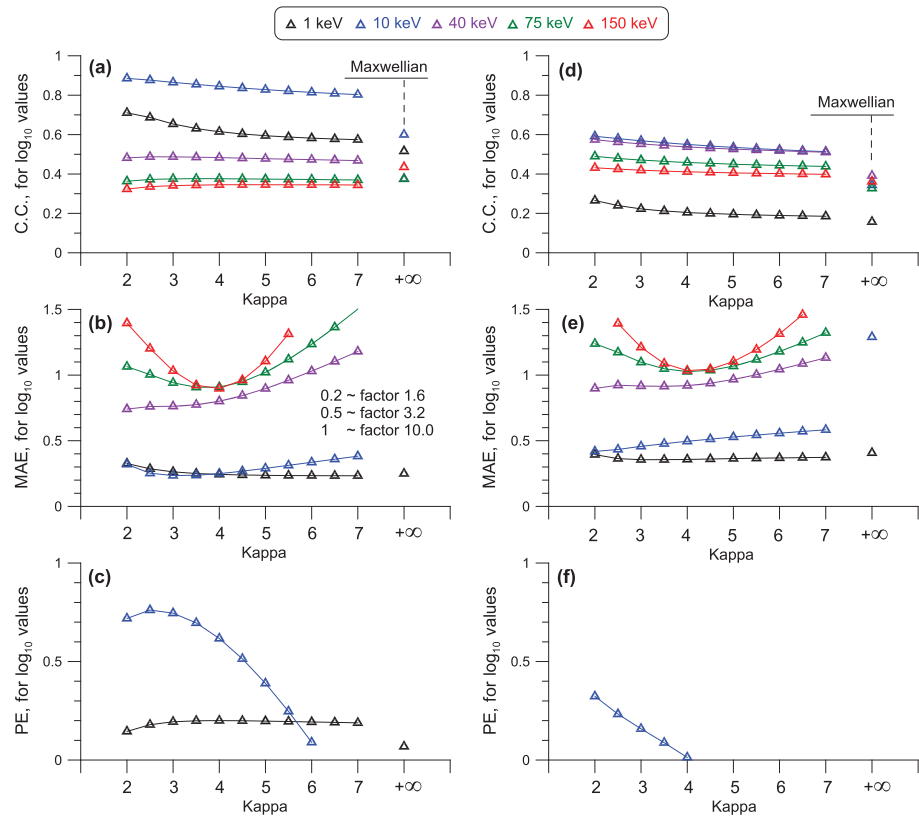
Figure 4. The correlation coefficient (CC), mean absolute error (MAE), and prediction efficiency (PE) computed for $\log_{10}$ values of measured and reconstructed energy flux. The density and temperature from the THEMIS data set were used for reconstruction in (a)–(c) while the Dubyagin et al. (2016) empirical model was used in (d)–(f).

its predictive ability is perfect. In other words, the difference of fluxes in Figure 3 stems entirely from the difference between the actual and assumed distribution functions with all additional errors, which could be possibly introduced by the empirical model of the temperature and density, excluded.

It can be seen that the high flux values in Figure 3a are generally in agreement, while significant disagreement is observed for the low fluxes. It can be speculated that the data records with low flux for 10 keV energy correspond to very low electron temperatures and large scatter is due to the incorrect representation of the superthermal tail of the spectra. However, the low fluxes represent only a minor part of the data set and that is confirmed by the high correlation coefficient, CC = 0.84, computed for $\log_{10}$ values of quantities in Figure 3a (since the fluxes vary over a few orders of magnitude, hereinafter we will use common logarithm values of fluxes for all metrics). Figure 3b shows the similar scatter plot for $E = 75$ keV. The agreement is obviously much worse (CC = 0.38).

We did the same comparison for various energies and κ parameter values and summarize the results in Figures 4a–4c.

The linear correlation coefficient (CC, Figure 4a), mean absolute error (MAE, Figure 4b), and prediction efficiency (PE, Figure 4c) are computed for $\log_{10}$ values of measured and reconstructed energy flux. The horizontal axis shows the κ parameter which was used for the flux reconstruction. Colors correspond to the energies (see legend at the top of the figure). The infinite value of κ corresponds to a Maxwellian distribution. The PE is computed as PE $= 1 - (\text{rms}/\sigma)^2$, where rms is a root-mean-square deviation between the measured and reconstructed flux, and σ is a standard deviation of the measured flux. To ease an interpretation of the MAE values in Figure 4b, which are computed for $\log_{10}$ values of the fluxes, we convert them to the corresponding factors (or ratio of the measured and reconstructed fluxes) in the legend. It can be seen that the correlation is relatively high for the thermal and slightly superthermal energies (1–10 keV, black and blue symbols), but it becomes lower than CC = 0.5 for $E \geq 40$ keV. The MAE values demonstrate an even more dramatic decrease in the accuracy with the energy increase; the average difference between the

measured and reconstructed flux is around a factor of 1.5 for $E \leq 10$ keV, but it grows to a factor of 10 for $E \geq 40$ keV. Finally, the PE is positive only for 1 and 10 keV energies, demonstrating that even the average values of the fluxes are better estimates than those reconstructed from density and temperature for the energies $E \geq 40$ keV. The correlation coefficients in Figure 4a reveal little dependence on κ parameter, while the MAE values reveal a clear minimum at $\kappa = 3$–4, especially for the superthermal energies. Maxwellian distribution shows the worst results (in terms of MAE and PE values) over the entire energy range. It should be mentioned that the flux estimation for the Maxwellian distribution for high energies (75 and 150 keV) sometimes (for the low-temperature values) led to floating underflow error. The metrics could not be calculated for such events, and hence they were excluded. For this reason, the metrics for the Maxwellian distribution are actually calculated for the smaller data set in comparison to those for the kappa distribution. It can explain a somewhat higher value of the correlation of the 75 and 150 keV flux for Maxwellian in Figure 4. On the other hand, the MAE values for the Maxwellian distribution for the energies greater than 10 keV are beyond the vertical axis limits, indicating very poor quality of the Maxwellian approximation for superthermal energies.

For comparison, in Figures 4d–4f we plot the same metrics but computed using T and N predicted by the Dubyagin et al. (2016) model. It should be noted that although the model was built from the same data set of the THEMIS T and N values which were used for flux reconstruction in Figures 3 and 4a–4c, it replaces the true values of T and N with their approximations, and this introduces additional error into the flux reconstruction. At the same time, these metrics represent the realistic quality of the flux reconstruction from this kind of empirical models. It is a bit surprising, but the model estimates give even higher correlation for the energies greater than or equal to 40 keV. However, the results for the thermal energies are much worse. As expected, the correlation coefficients are lower than 0.75 and 0.82 obtained in Dubyagin et al. (2016) for the predictions of temperature and density themselves. At the same time, MAE values are significantly higher than those in Figure 4b, demonstrating the decrease of the flux reconstruction accuracy when the real model of temperature and density is used. Finally, the PE is positive only for 10 keV energy.

4. Occurrence of Single- and Two-Population Distributions

In a collisionless space plasma, the particle energy spectra can be rather complex. In such a case, the energy distribution cannot be described using only two parameters: number density and temperature. In this section, we tried to improve the description of the spectra using more complex distributions. Each observed spectrum was fitted by single- and two-population distribution functions. Since the Maxwellian distribution showed worst results (especially for high-energy part of the spectra; see Figure 4), the single-population fit was done for the kappa distribution. For the two-population fit, we use the sum of Maxwellian and Kappa distributions.

$$f(E) = N_m \cdot f(E, T_m)^{maxwell} + N_k \cdot f(E, T_k, \kappa)^{kappa}, \tag{7}$$

where m and k subscripts correspond to Maxwellian and kappa distributions, respectively. We do not use double kappa distribution fit because preliminary tests showed that the parameter search often diverged for such approximation. Wang et al. (2007) mentioned having similar problem with a double kappa distribution fit for spectra averaged over a much longer interval than 1.6 min used in our study. That is, their spectra were more smooth and yet the fitting routine often could not converge.

The free parameters of the approximations were determined minimizing the rms computed for the logarithmic values of the flux

$$Err = \sqrt{\frac{1}{n} \sum_{i=1}^{n} \left(\log_{10} J_i^{obs} / J_i^{fit} \right)^2}, \tag{8}$$

where the summation is performed over the points of the spectra. The nonlinear parameters of the fit were determined using the downhill simplex algorithm (Nelder & Mead, 1965). Figure 5 shows examples of measured spectra and its approximations. The black symbols correspond to the THEMIS measurements. The blue and red curves show the single- and two-population fits, respectively. We also plotted the spectra for N and T values from the THEMIS data set: The solid and dashed thin black curves correspond to kappa ($\kappa = 4$) and Maxwellian distributions. The parameters determined from the fits and those computed from
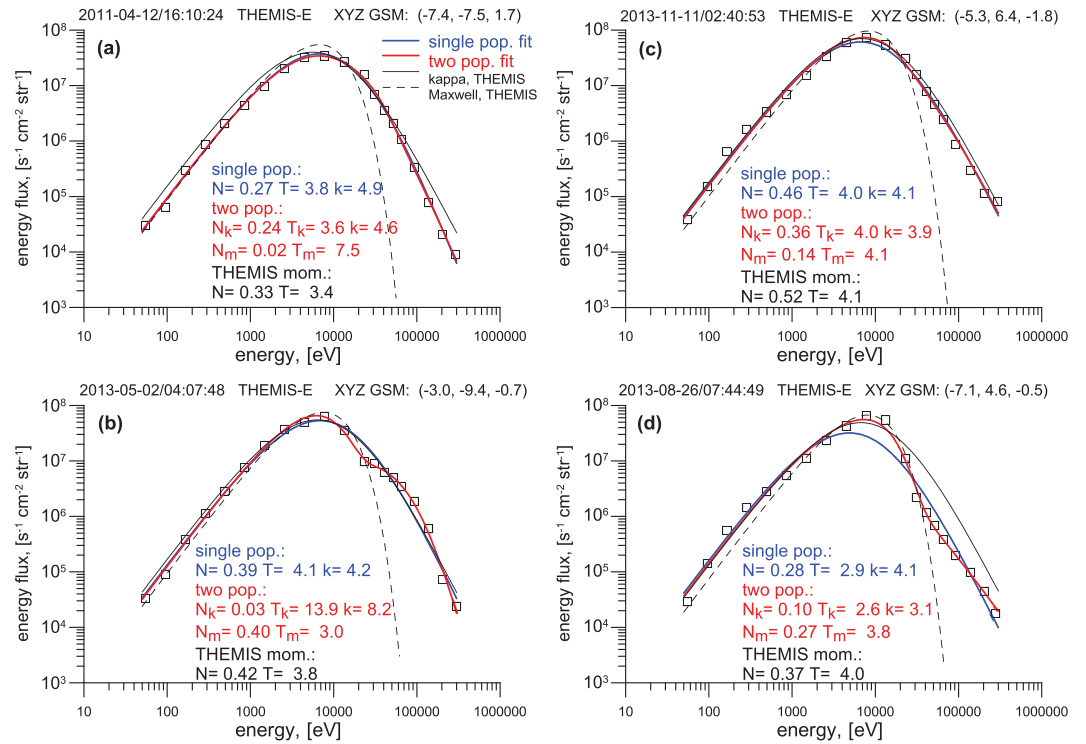
Figure 5. Examples of the measured spectra (black symbols) and approximations. Spectra in panels (a)–(d) are measured at different times and locations. Approximation parameters are given in the text box (N is in cm^{-3}, and T is in keV).

the THEMIS measurements are given in the legend. It can be seen that Maxwellian spectra plotted for measured N and T (dashed curve) is totally unable to describe the high energy part of the spectrum. The kappa distribution for the measured N and T (solid black curve) works better especially in Figure 5c. The single-population kappa fit works as well as the two-population fit in Figures 5a and 5c (note very low value for Maxwellian density, $N_m = 0.02 cm^{-3}$, in Figure 5a and close temperature of two populations, $T_k = 4$keV and $T_m = 4.1$keV, in Figure 5c). On the contrary, the two-population fit results in approximately 2 times smaller error than that for the single-population fit in Figures 5b and 5d (fit errors are not shown). Note that $T_k > T_m$ in Figure 5b and $T_k < T_m$ in Figure 5d.

Figure 6 shows the histograms of the errors for the single- and two-population approximations for six spatial bins (three bins in MLT and two bins in radial distance; the bin limits are shown in the legend). It can be seen that the histogram for the two-population approximation (red) peaks at almost 2 times lower error values than the histogram for the single population. To convert the logarithmic error to easier-to-interpret factor values, the $factor = 10^{Err}$ equation can be used. Thus, 0.05 and 0.1 logarithmic errors correspond to the average factors of 1.12 and 1.25, respectively. Note that since the logarithm in equation (8) is squared, this estimate cannot distinguish between the multiplier and divisor and the factor values greater than one do not imply flux underestimation.

To inspect the occurrence of the single- and two-population spectra, we calculated the ratio of errors of the single- and two-population fits. Figure 7 shows the histograms of the error ratio for the same spatial bins as in Figure 6. $Err1$ and $Err2$ refer to the errors of the single- and two-population approximations, respectively. Every histogram has a peak at $Err1/Err2 \approx 1$ corresponding to the events when two-population fit has not resulted in any improvements in comparison to the single-population fit. These peaks are especially evident in the duskside bins (Figures 7e and 7f) and the least pronounced for the inner/midnight bin (Figure 7d). The shaded area (and percentage) in the histograms corresponds to events with $Err1/Err2 > 2$, that is, when addition of the second population to the approximation reduces the error by factor 2 or more. The percentage of these events varies between 21% and 34%, being largest in the dawnside outer bin (Figure 7a). We also analyzed an order relation between T_m and T_k for two-population fits. It was found that for the events with
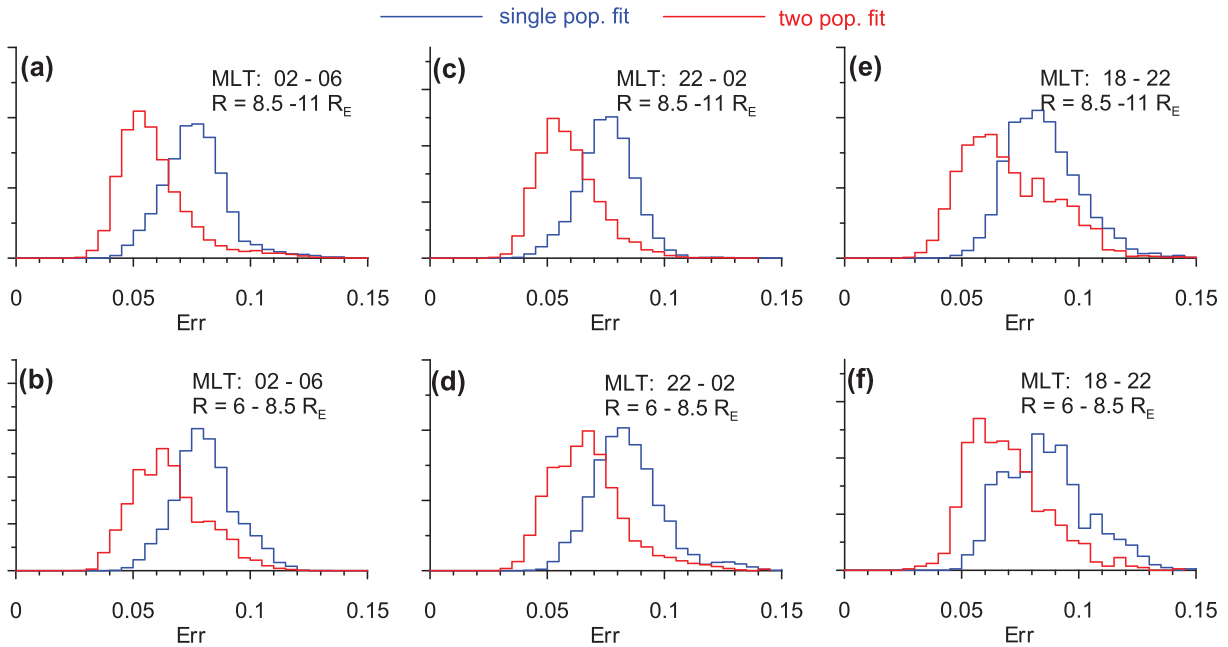
Figure 6. The histograms of the approximation errors for the single-population (blue) and two-population (red) fits. Panels (a)–(f) correspond to different MLT-R bins. The errors were calculated as RMS of the common logarithm values of the observed spectrum and its approximation.

$Err1/Err2 > 2$, the temperature of Maxwellian component is higher than that of kappa component for 72% of events. Finally, we investigated how the occurrence of two-population spectra depends on geomagnetic activity. We selected the subsets corresponding to the quiet periods, recovery, and main phases of the storms. The recovery and main phases were defined using criteria dSYM-H/dt > 0 and dSYM-H/dt < −0.1 nT/min, respectively, where the SYM-H derivative was calculated for the smoothed SYM-H series as described in Dubyagin et al. (2016). The quiet periods were selected using criteria SYM-H > −10 nT and |dSYM-H/dt| < 0.05 nT/min. We plotted the histograms of error ratio separately for these subsets (not shown) but found no big difference; the percentages of events with $Err1/Err2 > 2$ were 24%, 30%, and 28% for the quiet periods,
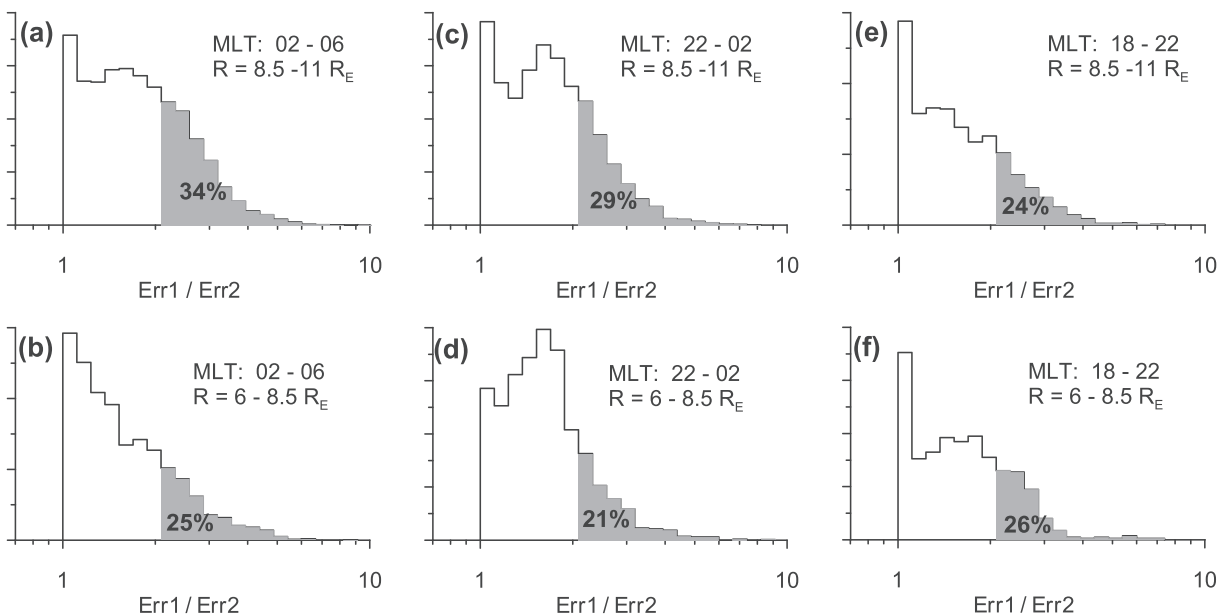
Figure 7. The histograms of the single- to two-population fit error ratio. Panels (a)–(f) correspond to different MLT-R bins. The errors were calculated as RMS of the common logarithm values of the observed spectrum and its approximation. The percentage of points with the ratio greater than two is shown.

main, and recovery phases, respectively. It can be seen that the percentage variability among these subsets is comparable to that for different MLT-R bins in Figure 7.

5. Kappa Parameter Values Inferred From the Observed Spectra

In this section, we analyze the statistical distribution of the kappa parameter obtained from fitting the spectra as described in section 4. However, the accuracy of the kappa parameter estimation using this method can be reduced by possible poor intercalibration of the SST and ESA detectors. For this reason, besides fitting a full observed spectrum with the kappa distribution, we tried alternative method to determine the κ parameter from the data of the SST detector alone. Since the energy flux for κ distribution at energies $E \gg T$ can be approximated as $J_E \sim E^{-\kappa+1}$ (see equations (5) and (6)), the κ parameter can be estimated from the slope of the spectra at high energies in double log scale (e.g. Åsnes et al., 2008; Gabrielse et al., 2014). We fitted the spectra by linear regression in double log scale for the energies greater than 40 keV, and the result is shown in Figure 8a. Although the histogram peaks at $\kappa = 3$–3.5, there are significant number of spectra producing very low kappa values ($\kappa < 2$; equation (5) is not valid for $\kappa \leq 1.5$). We do expect that this method can underestimate κ for the distributions with high temperatures. Numerical tests of the method with synthetic kappa spectra showed that the accuracy of kappa determination, apart from the temperature, depends also on the kappa itself (the method is less accurate for large kappa values). For example, for a distribution with $\kappa = 3$ and $T = 10$ keV the kappa is underestimated by 0.5, but for a distribution with $\kappa = 5$ the temperature should be less than 3 keV to keep the error within the same bounds. Although the histogram in Figure 2a shows that for majority of the spectra the electron temperature is well below 8 keV (that is, $\ll 40$ keV), it should be remembered that those temperatures can be underestimated due to the presence of the cold dense plasma as it was discussed in section 2.

Figure 8b shows the kappa values estimated using a single-population fit. It can be seen that the histogram has a peak at higher κ values in comparison to that obtained using the linear fit. Note, again, the significant fraction of events in the $\kappa < 2$ bin. To take into account spectra which cannot be described by a single-population distribution, we created a composite data set. For those events with $Err1$ to $Err2$ ratio less than 2 we took kappa values obtained from the single-population fit; otherwise, we took kappas from the two-population fits. The result is shown in Figure 8c. It can be seen that the histogram is wider in comparison to those above. The number of data points to the left from the histogram peak increased significantly, but the fraction of events in the $\kappa < 2$ bin is almost the same as in Figure 8b. In Figure 8d, we separately analyze the events when the two-population fit showed 2 times better accuracy than the single-population fit. The histogram has a sharp peak at $\kappa = 2.5$–3. It is at significantly lower kappa values than those in Figures 8b and 8c. To further investigate the two-population fits, we divided the obtained κ data set according to T_m and T_k order relation. Both subsets are shown in Figure 8e. It can be seen that the spectra with $T_m > T_k$ usually give lower kappa values, and such events comprise more than two thirds of all two-population fits having $Err1/Err2 > 2$.

Finally, we investigated the dependence of the κ parameter of the geomagnetic disturbance level and spatial location for three data sets: linear fit, single-population fit, and the composite data set. Figure 9 shows the kappa parameter versus MLT for two ranges of radial distance shown by red ($r = 6$–$8.5R_E$) and black ($r = 8.5$–$11R_E$). The median values are shown by the symbols, and two percentiles (15% and 85%) are shown by lines. All three data sets (Figures 9a–9b) demonstrate clear dependence of kappa values on MLT in the near-Earth region (red color), especially in the dusk-midnight sector. The kappa values outside $r = 8.5R_E$ (black color) reveal less pronounced, if any, MLT dependence. The linear regression fit to the median values gives azimuthal gradient values of $\Delta\kappa \approx 0.5$–0.6 per 6 hr of MLT for $r < 8.5R_E$ and $\Delta\kappa \approx 0.0$–0.3 per 6 hr of MLT for $r > 8.5R_E$. To investigate the radial dependence, we also plotted the kappa parameter versus radial distance for three MLT sectors (shown in supporting information Text S2). The median values revealed almost linear dependence on radial distance with radial gradient varying from 0.33–0.53 per $1R_E$ in the dusk MLT bin to 0.21–0.36 per $1R_E$ in the midnight and dawnside bins.

We also plotted κ versus SYM-H separately for quiet periods, recovery, and main phases of the storms (see supporting information Text S3). Surprisingly, we found no clear dependence on SYM-H, though the mean and median kappa values were somewhat lower for the recovery phase (~ 0.2–0.4 difference in κ values depending on chosen data set). However, it might be an effect of interference from the stronger MLT and
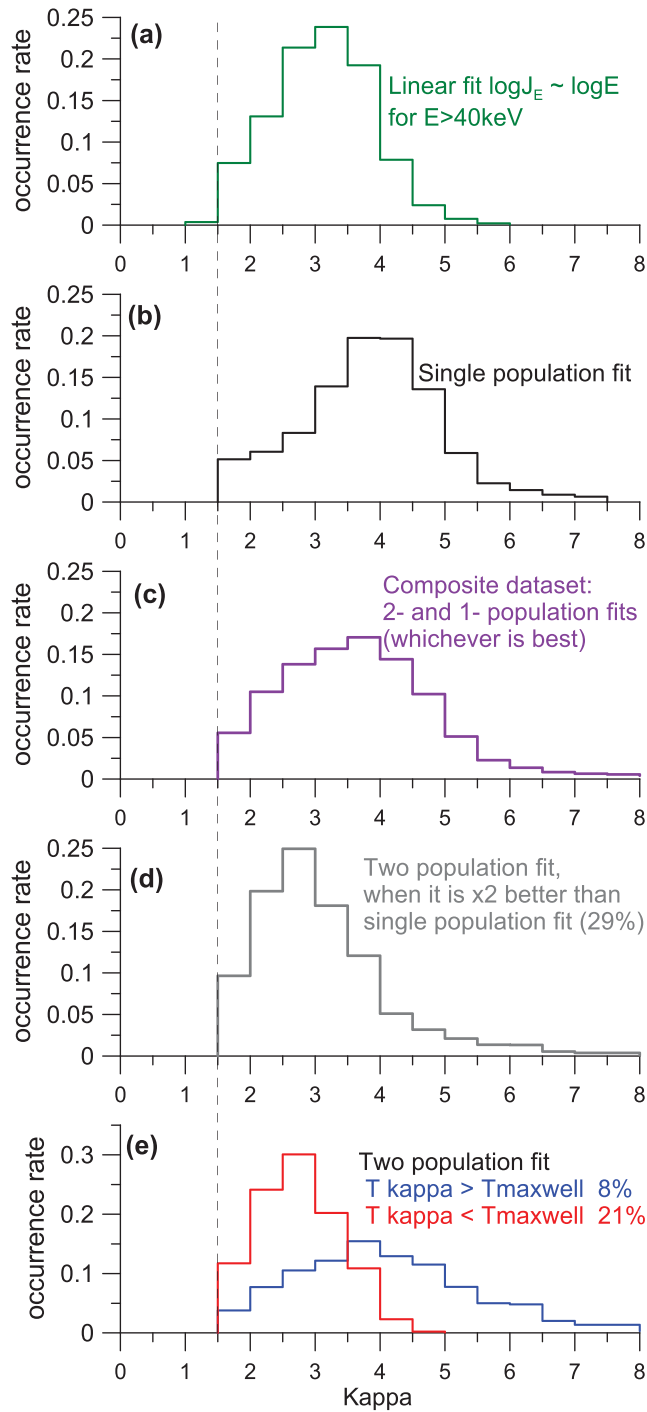
Figure 8. Histograms of the κ parameter obtained using different fits (panels (a)–(e)) of the observed spectra.

radial dependences due to inhomogeneity of the distribution of the observation points for the main and recovery phases (see supporting information Text S4).

6. Discussion

The goal of this study is to test the existing schemes of the outer boundary condition construction for the inner magnetosphere particle simulations, particularly, particle flux reconstruction from the temperature and density models. We have quantitatively tested the accuracy of the electron flux reconstruc-
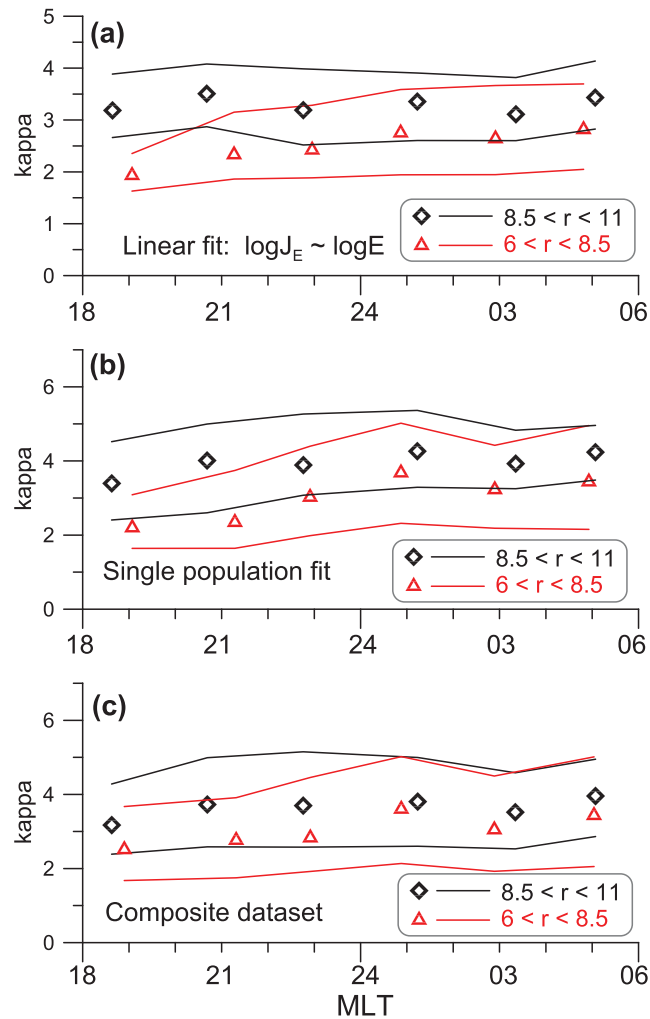
Figure 9. κ parameter versus MLT; median, 15%, and 85% percentiles are shown for two radial distance ranges: $r = 6$–$8.5R_E$ (red) and $r = 8.5$–$11R_E$ (black). The results are obtained using linear spectrum fit (a), single-population fit (b), and composite data set (c).

tion/prediction from the density and temperature models using standard Maxwell or kappa distributions. It turned out that the variety of the observed spectra cannot be described with acceptable accuracy by this simple method using a single-population distribution. It was shown in section 3 that even the average flux values provide better predictions than the fluxes reconstructed from the density and temperature values for the energies greater than 40 keV. This reflects the fact that the electron bulk properties are dominated by < 40 keV electrons. Therefore, any plasma sheet model based only on bulk properties is inherently insensitive to ≥ 40 keV electrons and therefore cannot be expected to predict them accurately in general. Further, we will discuss two possible ways how the improvement in this aspect can be achieved.

The first way is to develop an empirical model of the particle fluxes instead of the density and temperature models. This approach has already been implemented in its simplest form. For example, Chen et al. (2006) used Korth et al. (1999) flux model that represents MLT-dependent averaged spectra observed by LANL spacecraft at the geostationary orbit binned according to Kp level (energy range: ∼ 0.1–30 keV). Denton et al. (2016) presented a statistical model (it outputs mean, median, and percentiles) of the ion and electron fluxes at GEO (for 40 energies in the 1 eV to 40 keV range) binned according to MLT and solar wind electric field. Recently, Sillanpää et al. (2017) presented a model of the electron flux at the geostationary orbit for three energy channels (40, 75, and 159 keV) as a function of the solar wind parameters which also can be used as a boundary condition (for corresponding energy range).
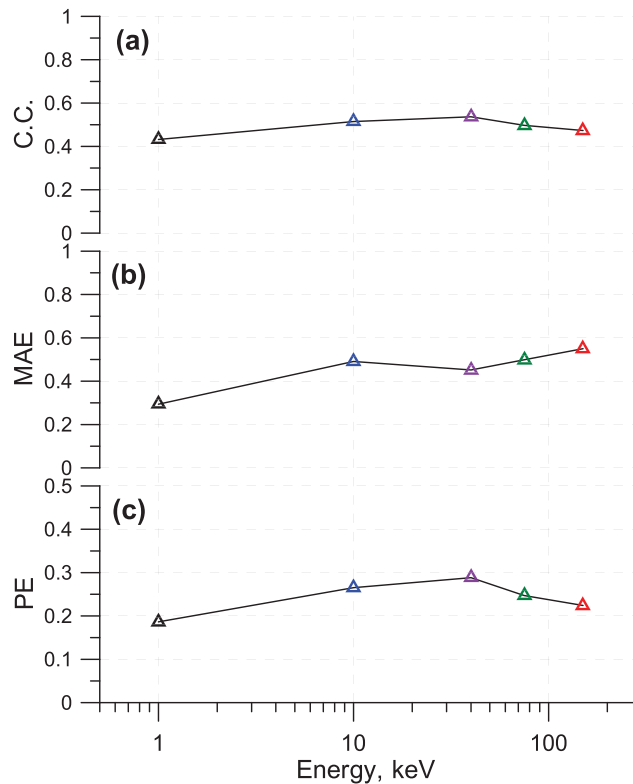
Figure 10. The quality metrics of the electron flux prediction versus energy: correlation coefficient (a), mean absolute error (b), and prediction efficiency (c). The flux predictions are obtained using the multiple linear regression with the input parameters of the (Dubyagin et al., 2016) model used as explanatory variables.

Trying to evaluate the possible gain in accuracy provided by a flux-based model in comparison to density and temperature models, we used simple multiple linear regression to describe the electron energy flux dependence on the external drivers. In this experiment, we use the input parameters of the Dubyagin et al. (2016) density and temperature models as external driving parameters (time averaged solar wind magnetic field and plasma parameters; five explanatory variables in total). The regressions were made for five energy channels. These regressions were used as a model of the electron energy flux and their predictions (along with observations) were used to calculate the same quality metrics as we did in section 3. The obtained correlation coefficients, MAE, and PE values are presented in Figure 10. It can be seen that all metrics are prominently better than those in Figures 4d–4f. The main improvement is achieved for the superthermal energies.

It should be noted that we have not searched for the optimal driving parameters, nor have we checked if the dependencies were linear, and the dependence on spatial coordinates has not been included either. If these measures were taken, the resulting metrics certainly would be much better.

Another way to enhance the flux boundary condition is to introduce additional parameters to the modeled energy distribution function. Figure 4 clearly demonstrates that the fixed values of the kappa parameter cannot provide acceptable accuracy of flux estimations at superthermal energies. On the other hand, we found that the kappa parameter shows strong dependence on MLT and radial distance with spectra being harder (κ being lower) in the dusk sector and closer to the Earth (see section 5). The same dependences can be traced in two-dimensional equatorial plots of the kappa parameter in Espinoza et al. (2018). Although the authors also use THEMIS data, a validity of the results can be independently confirmed by general agreement of the averaged kappa values with that obtained by Christon et al. (1991) using ISEE 1 data at $r > 12R_E$. This spatial dependence of κ parameter can be modeled empirically in addition to the density and temperature.

Finally, an empirical model of the additional second population can be added. Previous studies showed that the multiple plasma populations are not uncommon for the midtail plasma sheet (Fujimoto et al., 1998; Hasegawa et al., 2004; Liemohn & Welling, 2016; Walsh et al., 2013; Wang et al., 2007; Wang et al., 2012;

Wing et al., 2005) where a cold component likely penetrates from the low-latitude boundary layer and is mixed with the more energetic plasma sheet population. It was however surprising to discover that the electron spectra at the boundary of the inner magnetosphere reveal two-population features for $\sim 1/5$–$1/3$ of events (depending on the location and disturbance level, see section 4). It can be speculated that for some fraction of these events, two-population-like appearance of the spectra is a result of poor intercalibration between the ESA and SST detectors due to the large energy gap between the ESA and SST energy ranges. For example, if the SST fluxes were underestimated, it would result in local steep decrease of the spectra with increasing energy in the vicinity of ~ 30 keV and harder spectra at higher energies. In this case, this artificial localized steepening of the spectrum can be described by an additional Maxwellian distribution. However, the similar features of the electron spectra were observed by Christon et al. (1991) on ISEE 1, where the energy ranges of the low- and high-energy detectors overlapped, and the intercalibration was not an issue. One more question that should be addressed before implementing a two-population empirical model is the conditions when a second population should be switched on. Our results indicate that the single- and two-population distributions both can be observed on the nightside between 6 and $11R_E$ with comparable probability. At the same time we could not discriminate these two groups using location or geomagnetic activity parameters, and this is the task for future studies. It also should be noted that the criterion for the two- and single-population spectra discrimination ($Err1/Err2 > 2$) is somewhat arbitrary and should be defined in a more substantiated way for future studies.

Note that the majority of the strategies which were outlined above are difficult or impossible to apply to the boundary condition constructed using the input from MHD simulations (e.g. Buzulukova et al., 2010; De Zeeuw et al., 2004; Toffoletto et al., 2004) because density, temperature, and bulk plasma velocity are the only plasma characteristics MHD deals with. At the same time, the necessity of improving the boundary condition driven by MHD simulations was recently demonstrated (Yu et al., 2019). Some improvement can be achieved using a combination of the MHD temperature and density output and empirical model of the spatial coordinate dependent kappa parameter. In addition, the spectral properties of the energy distribution can depend on the temperature and density themselves. We do find significant correlation (CC = 0.47) between the kappa parameter and temperature. On the other hand, the MHD simulations have an advantage which the empirical models of the plasma parameters do not have: Their plasma parameters are self-consistent with the magnetic field. Gabrielse et al. (2014),Runov et al. (2015) found that the electrons intruding into the inner magnetosphere with dipolarized flux bundles have softer spectra (higher κ values) than the background population; that is, the spectral properties of the electrons depend on the local magnetic and electric fields. This dependence can be used to correct the fluxes reconstructed from the MHD density and temperature using MHD magnetic and electric fields. Even if the MHD simulation cannot accurately predict the timing of the dipolarization events during the substorms, the self-consistent input of the particle content to the inner magnetosphere can potentially result in more realistic fluxes there, at least in a statistical sense.

The results of our study are also worth discussing in the context of the surface charging analysis. It has been established that the high flux of electrons with energies $E \geq 10$ keV is the main factor leading to the hazardous level of surface charging (e.g Thomsen et al., 2013; Ferguson et al., 2015; Matéo-Vélez et al., 2018). Some engineering systems of the surface charging modeling use the density and temperature of the plasma environment as an input. Figure 4 demonstrated that the kappa distribution represents the flux at 10 keV energy reasonably well for the THEMIS storm time data set. However, the errors of flux estimations made with the Maxwell distribution are on average beyond 1 order of magnitude difference. To further investigate the difference of the Maxwell and kappa flux estimates, we performed numerical test calculating the integrated number flux of 10–50 keV electrons for the kappa and Maxwell distributions for different electron temperatures and kappa parameters. It turned out that the difference between the kappa and Maxwellian flux is negligible for $T_e > 3$ keV, but it grows fast with the temperature decreasing and reached 1, 2 orders of magnitude at $T_e = 1$ keV for $\kappa = 10$ and $\kappa = 2$, respectively. On the other hand, the surface charging events are usually associated with high electron temperature values, for which we expect that the electron flux is reproduced with reasonable accuracy even for the Maxwellian distribution.

7. Conclusion

We conducted an examination of the accuracy of representing plasma sheet electron fluxes from empirical models based on moment values and also from the moments of the local flux spectra themselves. By analyzing 7 years of data from the THEMIS mission spacecraft on the nightside between $r = 6$ and $r = 11R_E$, combining the fluxes measured by the ESA and SST instruments, we found the following:

1. The electron flux can be accurately (within a factor 2) estimated from the number density and temperature only at thermal and slightly superthermal energies. For higher energies ($E > 10$ keV), the error grows fast and the average error is greater than an order of magnitude for $E > 40$ keV.
2. The optimal fixed κ parameter for the electron flux estimation is $\kappa = 3$–4, but it reveals strong dependence on MLT and the radial distance.
3. The electron spectra reveal two-population features for $\sim 1/5$–$1/3$ of all observations depending on location and geomagnetic disturbance level.
4. A promising way to improve the flux estimation accuracy is development of "flux-based" model, that is, the model of the differential particle flux for selected reference energies; the continuous spectrum can be obtained using interpolation.

References

Angelopoulos, V. (2008, Apr 22). The THEMIS mission. *Space Science Reviews*, *141*, 5–34. https://doi.org/10.1007/s11214-008-9336-1

Angelopoulos, V., Sibeck, D., Carlson, C. W., McFadden, J. P., Larson, D., Lin, R. P., et al. (2008, Dec 01). First results from the THEMIS mission. *Space Science Reviews*, *141*(1), 453–476. https://doi.org/10.1007/s11214-008-9378-4

Åsnes, A., Friedel, R. W. H., Lavraud, B., Reeves, G. D., Taylor, M. G. G. T., & Daly, P. (2008). Statistical properties of tail plasma sheet electrons above 40 keV. *Journal of Geophysical Research*, *113*, A03202. Retrieved from, https://doi.org/10.1029/2007JA012502

Auster, H. U., Glassmeier, K. H., Magnes, W., Aydogar, O., Baumjohann, W., Constantinescu, D., et al. (2008, Dec 01). The THEMIS fluxgate magnetometer. *Space Science Reviews*, *141*(1), 235–264. https://doi.org/10.1007/s11214-008-9365-9

Buzulukova, N., Fok, M.-C., Pulkkinen, A., Kuznetsova, M., Moore, T. E., Glocer, A., & Rastätter, L. (2010). Dynamics of ring current and electric fields in the inner magnetosphere during disturbed periods: CRCM-BATS-R-US coupled model. *Journal of Geophysical Research*, *115*, A05210. https://doi.org/10.1029/2009JA014621

Chen, M. W., Liu, S., Schulz, M., Roeder, J. L., & Lyons, L. R. (2006). Magnetically self-consistent ring current simulations during the 19 October 1998 storm. *Journal of Geophysical Research*, *111*, A11S15. https://doi.org/10.1029/2006JA011620

Christon, S. P., Williams, D. J., Mitchell, D. G., Huang, C. Y., & Frank, L. A. (1989). Spectral characteristics of plasma sheet ion and electron populations during undisturbed geomagnetic conditions. *Journal of Geophysical Research Space Physics*, *94*(A10), 13,409–13,424. https://doi.org/10.1029/JA094iA10p13409

Christon, S. P., Williams, D. J., Mitchell, D. G., Huang, C. Y., & Frank, L. A. (1991). Spectral characteristics of plasma sheet ion and electron populations during disturbed geomagnetic conditions. *Journal of Geophysical Research*, *96*(A1), 1–22. https://doi.org/10.1029/90JA01633

De Zeeuw, D. L., Sazykin, S., Wolf, R. A., Gombosi, T. I., Ridley, A. J., & Tóth, G. (2004). Coupling of a global MHD code and an inner magnetospheric model: Initial results. *Journal of Geophysical Research*, *109*, A12219. https://doi.org/10.1029/2003JA010366

Denton, M. H., Henderson, M. G., Jordanova, V. K., Thomsen, M. F., Borovsky, J. E., Woodroffe, J., et al. (2016). An improved empirical model of electron and ion fluxes at geosynchronous orbit based on upstream solar wind conditions. *Space Weather*, *14*, 511-523. Retrieved from, https://doi.org/10.1002/2016SW001409

Dubyagin, S., Ganushkina, N. Y., Sillanpää, I., & Runov, A. (2016). Solar wind- driven variations of electron plasma sheet densities and temperatures beyond geostationary orbit during storm times. *Journal of Geophysical Research: Space Physics*, *121*, 8343–8360. https://doi.org/10.1002/2016JA022947

Espinoza, C. M., Stepanova, M., Moya, P. S., Antonova, E. E., & Valdivia, J. A. (2018). Ion and electron κ distribution functions along the plasma sheet. *Geophysical Research Letters*, *45*, 6362–6370. https://doi.org/10.1029/2018GL078631

Ferguson, D., Hilmer, R., & Davis, V. (2015, 03). Best Geosynchronous Earth Orbit daytime spacecraft charging index. *Journal of Spacecraft and Rockets*, *52*, 526–543 doi: https://doi.org/10.2514/1.A32959.

Fok, M.-C., Buzulukova, N. Y., Chen, S.-H., Glocer, A., Nagai, T., Valek, P., & Perez, J. D. (2014). The comprehensive inner magnetosphere-ionosphere model. *Journal of Geophysical Research: Space Physics*, *119*, 7522–7540. https://doi.org/10.1002/2014JA020239

Fok, M.-C., Moore, T. E., & Spjeldvik, W. N. (2001). Rapid enhancement of radiation belt electron fluxes due to substorm dipolarization of the geomagnetic field. *Journal of Geophysical Research*, *106*, 3873–3881. https://doi.org/10.1029/2000JA000150

Fok, M.-C., Wolf, R. A., Spiro, R. W., & Moore, T. E. (2001). Comprehensive computational model of Earth's ring current. *Journal of Geophysical Research Space Physics*, *106*(A5), 8417–8424. https://doi.org/10.1029/2000JA000235

Fujimoto, M., Terasawa, T., Mukai, T., Saito, Y., Yamamoto, T., & Kokubun, S. (1998). Plasma entry from the flanks of the near-Earth magnetotail: Geotail observations. *Journal of Geophysical Research*, *103*(A3), 4391–4408. Retrieved from, https://doi.org/10.1029/97JA03340

Gabrielse, C., Angelopoulos, V., Runov, A., & Turner, D. L. (2014). Statistical characteristics of particle injections throughout the equatorial magnetotail. *Journal of Geophysical Research: Space Physics*, *119*, 2512-2535. Retrieved from, https://doi.org/10.1002/2013JA019638

Ganushkina, N. Y., Amariutei, O. A., Shprits, Y. Y., & Liemohn, M. W. (2013). Transport of the plasma sheet electrons to the geostationary distances. *Journal of Geophysical Research: Space Physics*, *118*, 82–98. https://doi.org/10.1029/2012JA017923

Ganushkina, N. Y., Liemohn, M. W., Amariutei, O. A., & Pitchford, D. (2014). Low-energy electrons (5-50 keV) in the inner magnetosphere. *Journal of Geophysical Research: Space Physics*, *119*, 246–259. https://doi.org/10.1002/2013JA019304

Ganushkina, N. Y., Pulkkinen, T. I., Milillo, A., & Liemohn, M. (2006). Evolution of the proton ring current energy distribution during 21–25 April 2001 storm. *Journal of Geophysical Research*, *111*, A11S08. https://doi.org/10.1029/2006JA011609

Harel, M., Wolf, R. A., Reiff, P. H., Spiro, R. W., Burke, W. J., Rich, F. J., & Smiddy, M. (1981). Quantitative simulation of a magnetospheric substorm 1. Model logic and overview. *Journal of Geophysical Research*, *86*(A4), 2217–2241. https://doi.org/10.1029/JA086iA04p02217

Hasegawa, H., Fujimoto, M., Saito, Y., & Mukai, T. (2004). Dense and stagnant ions in the low-latitude boundary region under northward interplanetary magnetic field. *Geophysical Research Letters*, *31*, L06802. https://doi.org/10.1029/2003GL019120

Jordanova, V. K., Boonsiriseth, A., Thorne, R. M., & Dotan, Y. (2003). Ring current asymmetry from global simulations using a high-resolution electric field model. *Journal of Geophysical Research*, *108*(A12), 1443. https://doi.org/10.1029/2003JA009993

Jordanova, V. K., Kistler, L. M., Thomsen, M. F., & Mouikis, C. G. (2003). Effects of plasma sheet variability on the fast initial ring current decay. *Geophysical Research Letters*, *30*(6), 1311. https://doi.org/10.1029/2002GL016576

Jordanova, V. K., & Miyoshi, Y. (2005). Relativistic model of ring current and radiation belt ions and electrons: Initial results. *Geophysical Research Letters*, *32*, L14104. https://doi.org/10.1029/2005GL023020

Jordanova, V. K., Yu, Y., Niehof, J. T., Skoug, R. M., Reeves, G. D., Kletzing, C. A., et al. (2014). Simulations of inner magnetosphere dynamics with an expanded RAM-SCB model and comparisons with Van Allen Probes observations. *Geophysical Research Letters*, *41*, 2687–2694. https://doi.org/10.1002/2014GL059533

Korth, H., Thomsen, M. F., Borovsky, J. E., & McComas, D. J. (1999). Plasma sheet access to geosynchronous orbit. *Journal of Geophysical Research*, *104*(A11), 25,047–25,061. https://doi.org/10.1029/1999JA900292

Liemohn, M. W., & Welling, D. T. (2016). Ionospheric and solar wind contributions to magnetospheric ion density and temperature throughout the mag- netotail, in *Magnetosphereionosphere coupling in the solar system*. American Geophysical Union (AGU), 101–114 Retrieved from, https://doi.org/10.1002/9781119066880.ch8

Livadiotis, G. (2015). Introduction to special section on origins and properties of kappa distributions: Statistical background and properties of kappa distributions in space plasmas. *Journal of Geophysical Research: Space Physics*, *120*, 1607–1619. https://doi.org/10.1002/2014JA020825

Matéo-Vélez, J.-C., Sicard, A., Payan, D., Ganushkina, N., Meredith, N. P., & Sillanpää, I. (2018). Spacecraft surface charging induced by severe environments at geosynchronous orbit. *Space Weather*, *16*, 89-106. Retrieved from, https://doi.org/10.1002/2017SW001689

McFadden, J. P., Carlson, C. W., Larson, D., Bonnell, J., Mozer, F., Angelopou-los, V., et al. (2008, Dec 01). THEMIS ESA first science results and performance issues. *Space Science Reviews*, *141*(1), 477–508. https://doi.org/10.1007/s11214-008-9433-1

McFadden, J. P., Carlson, C. W., Larson, D., Ludlam, M., Abiad, R., Elliott, B., & Angelopoulos, V. (2008, Dec 01). The THEMIS ESA plasma instrument and in-flight calibration. *Space Science Reviews*, *141*(1), 277–302. https://doi.org/10.1007/s11214-008-9440-2

Nelder, J. A., & Mead, R. (1965). A simplex method for function minimization. *The Computer Journal*, *7*(4), 308–313. https://doi.org/10.1093/comjnl/7.4.308

Paschmann, G., & Daly, P. (1998). *Analysis methods for multi-spacecraft data*. Bern, Switzerland: International Space Science Institute.

Runov, A., Angelopoulos, V., Gabrielse, C., Liu, J., Turner, D. L., & Zhou, X.-Z. (2015). Average thermodynamic and spectral properties of plasma in and around dipolarizing flux bundles. *Journal of Geophysical Research: Space Physics*, *120*, 4369–4383. https://doi.org/10.1002/2015JA021166

Sillanpää, I., Ganushkina, N. Y., Dubyagin, S., & Rodriguez, J. V. (2017). Electron fluxes at geostationary orbit from GOES MAGED data. *Space Weather*, *15*, 1602–1614. https://doi.org/10.1002/2017SW001698

Thomsen, M. F., Bame, S. J., McComas, D. J., Moldwin, M. B., & Moore, K. R. (1994). The magnetospheric lobe at geosynchronous orbit. *Journal of Geophysical Research*, *99*(A9), 17,283–17,293. https://doi.org/10.1029/94JA00423

Thomsen, M. F., Henderson, M. G., & Jordanova, V. K. (2013). Statistical properties of the surface-charging environment at geosynchronous orbit. *Space Weather*, *11*, 237-244. Retrieved from, https://doi.org/10.1002/swe.20049

Toffoletto, F., Sazykin, S., Spiro, R., & Wolf, R. (2003). Inner magnetospheric modeling with the rice convection model. *Space Science Reviews*, *107*(1), 175,196–175,196. https://doi.org/10.1023/A:1025532008047

Toffoletto, F., Sazykin, S., Spiro, R., Wolf, R., & Lyon, J. (2004). RCM meets LFM: initial results of one-way coupling. *Journal of Atmospheric and Solar - Terrestrial Physics*, *66*(15), 1361–1370. (Towards an Integrated Model of the Space Weather System), https://doi.org/10.1016/j.jastp.2004.03.022

Vasyliunas, V. M. (1968). A survey of low-energy electrons in the evening sector of the magnetosphere with OGO 1 and OGO 3. *Journal of Geophysical Research*, *73*(9), 2839–2884. https://doi.org/10.1029/JA073i009p02839

Walsh, A. P., Fazakerley, A. N., Forsyth, C., Owen, C. J., Taylor, M. G. G. T., & Rae, I. J. (2013). Sources of electron pitch angle anisotropy in the magnetotail plasma sheet. *Journal of Geophysical Research: Space Physics*, *118*, 6042–6054. Retrieved from, https://doi.org/10.1002/jgra.50553

Wang, C.-P., Gkioulidou, M., Lyons, L. R., & Angelopoulos, V. (2012). Spatial distributions of the ion to electron temperature ratio in the magnetosheath and plasma sheet. *Journal of Geophysical Research*, *117*, A08215. https://doi.org/10.1029/2012JA017658

Wang, C.-P., Lyons, L. R., Nagai, T., Weygand, J. M., & McEntire, R. W. (2007). Sources, transport, and distributions of plasma sheet ions and electrons and dependences on interplanetary parameters under northward interplanetary magnetic field. *Journal of Geophysical Research*, *112*, A10224. https://doi.org/10.1029/2007JA012522

Wing, S., Johnson, J. R., Newell, P. T., & Meng, C.-I. (2005). Dawn-dusk asymmetries, ion spectra, and sources in the northward interplanetary magnetic field plasma sheet. *Journal of Geophysical Research*, *110*, A08205. https://doi.org/10.1029/2005JA011086

Xiao, F., Shen, C., Wang, Y., Zheng, H., & Wang, S. (2008). Energetic electron distributions fitted with a relativistic kappa-type function at geosynchronous orbit. *Journal of Geophysical Research*, *113*, A05203. https://doi.org/10.1029/2007JA012903

Yu, Y., Rastätter, L., Jordanova, V. K., Zheng, Y., Engel, M., Fok, M.-C., & Kuznetsova, M. M. (2019). Initial results from the GEM challenge on the spacecraft surface charging environment. *Space Weather*, *17*, 299-312. Retrieved from, https://doi.org/10.1029/2018SW002031